

# Model based inversion for deriving maps of histological parameters characteristic of cancer from *ex-vivo* multispectral images of the colon

Ela Claridge and Džena Hidović-Rowe

**Abstract**— A model-based inversion method was used to obtain quantitative estimates of histological parameters from multispectral images of the colon and to examine their potential for discriminating between normal and pathological tissues. Pixel-wise estimates of the mucosal blood volume fraction, density of the scattering particles and thickness were derived using a two-stage method. In the first (forward) stage reflectance spectra corresponding to given instances of the parameter values were computed using Monte Carlo simulation of photon propagation through a multi-layered tissue. In the second (inversion) stage the parameter values were obtained via optimisation using an Iterated Conditional Modes (ICM) algorithm based on Discrete Markov Random Fields (DMRF). The method was validated on computer generated data contaminated with noise giving a mean normalized root-mean-square deviation (NRMSD) of 2.04. Validation on *ex vivo* images demonstrated that parametric maps show gross correspondence with histological features of mucosa characteristic of cancerous, pre-cancerous and non-cancerous colon lesions. The key signs of abnormality were shown to be the increase in the blood volume fraction and decrease in the density of scattering particles.

**Index Terms**—Colon cancer; Multispectral imaging; Inverse problems; Diffuse reflectance model; Monte Carlo simulation; Discrete Markov Random Fields.

## I. INTRODUCTION

### A. General

White light endoscopy, which is the most commonly used method for diagnosis of colon disorders, is unable to differentiate between different types of lesions and polyps. Flat and depressed lesions, which are often precursors of cancer, are particularly hard to detect due to their inconspicuous colour and non-elevated contour. If a lesion is discovered during endoscopic examination it is biopsied and a resected sample is analysed in a histopathology laboratory to assess its type and cancerous potential. Biopsy is an invasive

procedure which carries a rare but serious risk of colon perforation and non-invasive alternatives have been sought using a number of modalities including x-ray CT, ultrasound and optical imaging [1] [2].

One of such modalities is multispectral imaging which captures optical information at many different narrow wavebands of light. In this way it extends the capabilities of conventional colour imaging where images are acquired in the three broad bands: red, green and blue. Visible light (c. 400-700nm) can penetrate tissue to a depth of up to 4mm [3] so that the re-emitted signal carries information not just from the surface of the tissue but also from its near-surface interior. The blue light (c. 400-500nm) interrogates primarily superficial layers whereas red light (c. 600-700nm) can reach deeper layers. These different depths of penetration arise from generic properties of light scatter where, in accordance with the laws of physics, shorter (blue) wavelengths are scattered more strongly than longer (red) wavelengths. Light scattering is also a function of the size and density of the scattering particles present in the tissue such as collagen fibres and fibrils, cells and organelles. In most living tissues light is partially absorbed by the blood-borne pigments haemoglobin and oxyhaemoglobin whose absorption is wavelength dependent. When tissue is illuminated the light undergoes scattering and absorption, the amounts of which depend on the tissue structure and its pigment contents. As disease changes tissue histology it is also likely to change the spectral fingerprint of the light remitted from the tissue. Multispectral images, which contain spectral information at each image point, can be analysed to draw conclusions about the health of a tissue.

Interpretation of multispectral images often employs statistical methods that operate directly on the measured spectra. Such an approach has been long practised in remote sensing, where image regions are classified into various terrain or vegetation types based on their spectral signatures. This paper presents a different approach where spectral data is interpreted in terms of the underlying tissue histology. Such interpretation is possible through the use of a physics-based model of light interaction with colon tissue. Using a Monte Carlo (MC) model to simulate light-tissue interactions, parameters which describe the optical properties of tissue are correlated with the spectral composition of light observed at the surface after penetrating the tissue and interacting with its

Copyright (c) 2010 IEEE. Personal use of this material is permitted. However, permission to use this material for any other purposes must be obtained from the IEEE by sending a request to [pubs-permissions@ieee.org](mailto:pubs-permissions@ieee.org).

This work was supported in part by the U.K. Engineering and Physical Sciences Research Council studentship.

E. Claridge is with the School of Computer Science, University of Birmingham, Birmingham B15 2TT U.K. (e-mail: [e.claridge@cs.bham.ac.uk](mailto:e.claridge@cs.bham.ac.uk)).

D. Hidović-Rowe was with the School of Computer Science, University of Birmingham, Birmingham B15 2TT, U.K..

structure. The spectra obtained at each point of a multispectral image are then interpreted by the inversion of the model. The result is a set of parametric maps which show the spatial distribution, relative quantities of blood and the density and thickness of the collagen matrix in the topmost layer of the colon, the mucosa.

The work presented in this paper was undertaken to examine whether pathological changes, which may be invisible to standard endoscopy, can be captured through such model-based analysis and interpretation. Section II summarises a method of constructing a forward model of colon tissue. A method of extracting histological parameters from the spectra and its validation are presented in section III. Section IV describes experiments on *ex vivo* tissue samples. Results and their analysis are presented in section V. The paper ends with discussion and conclusions in sections VI and VII.

### B. Related work

The approach described in this paper builds upon earlier work on skin cancer imaging [3] and retinal imaging [4] [5] where a physics-based model of image formation was used successfully to derive histological information from multispectral images of the tissues. Hidovic & Claridge defined and validated a forward model of diffuse spectral reflectance for the colon [6] and demonstrated that their model correctly predicts spectral changes associated with the increase in the blood volume fraction in colon cancers [7].

Earlier on a number of groups working on the detection of pathologies of the gastrointestinal tract employed statistical analysis for classification of the diffuse reflectance spectra collected by an optical probe. Mourant *et al.* [8] obtained spectral measurements using an endoscope-compatible optical probe whose geometry was optimised for the detection of changes in morphology, size and shape of scattering centres. The algorithm to distinguish between normal and abnormal tissues compared spectral reflectance from the 540nm - 580nm region to the 400nm and 440nm region. Pathological samples tended to have lower reflectance in the 400-440nm range and higher in the 540-580 range. Ge *et al.* [9] studied diffuse reflectance spectroscopy of colon tissue with the aim of identifying colon dysplasia and neoplasia *in vivo*. Point spectra from normal mucosa, adenomatous polyps, hyperplastic polyps and adenocarcinoma were collected in the range of 350 - 800 nm. Classification to distinguish adenomatous polyps from hyperplastic polyps was carried out using multiple linear regression, linear discriminate analysis and back-propagating neural networks achieving predictive accuracy of 85%. Sambongi *et al.* [10] collected reflectance spectra from both normal tissue and early carcinoma using an endoscopic spectroscopy system. The measured spectra were normalised with respect to a long wavelength (640nm) and also the mean spectrum of the normal tissue. A linear analysis showed significant differences between normal tissue and early cancer.

Zonios, Perelman, Backman *et al.* [11] used a simplified light diffusion model of light propagation in colon to quantify haemoglobin concentration, oxygen saturation, scatterer density and scatterer size from the diffuse reflectance point collected by an optical probe from an *in vivo* colon. This approach was very different to the above statistical analysis applied purely to spectral data. Through their use of the model spectral changes could be attributed to changes in the optical and morphological characteristics of the tissue. The key finding of the paper was that haemoglobin concentration was significantly increased at adenocarcinoma sites in comparison to the normal tissue. The paper implemented an analytical solution to the light transport equation and therefore the model inversion could be computed analytically.

Gaelano *et al.* [12] have developed a forward diffuse reflectance model based on that by Zonios *et al.* but they did not use its inverse analytical formulation. Instead they performed inversion by spectral matching using genetic algorithms. They computed parametric maps of haemoglobin concentration, haemoglobin saturation, diameter of collagen fibres and volume fraction of collagen from the excised colon tissue samples showing differences between the normal tissue and pathological tissue.

Recent work of Antonelli *et al.* [13] exploited the differential depolarisation of light by different microscopic elements of the epithelial colon tissue. Image data was collected using a multispectral Mueller polarimetric imaging system. Experiments on excised colon tissue showed differences in depolarisation depending on cellular density, the nature of cancer (penetrating or budding), the presence of ulcerations, tumour thickness and the depth of its penetration to sub-mucosal layers.

The detection of pre-malignant changes in the colon is attracting much attention in the light of the high prevalence of colorectal cancers [1, 2] and increased survival rate if such changes are detected sufficiently early. A number of imaging methods are becoming available to aid the clinician. Chromoendoscopy, where colon tissue is stained with a contrasting agent such as methylene blue, is already used in the clinics as it does not require additional endoscopic instrumentation or post-processing; by enhancing structural details of the mucosa it increases visibility of subtle changes such as flat lesions or distorted mucosal pits [1]. Narrow band imaging (NBI) uses an additional (to RGB) imaging band in the blue end of the spectrum (380–450nm) to emphasise vascular features [14]. Confocal fluorescence endoscopy [15] [16] is a novel technology used in Cellvisio® (Mauna Kea Technologies S.A.). Other methods that are still at the development stage include Raman spectroscopy [17], point fluorescence endoscopy [18], optical coherence tomography [19]. Reviews of these methods can be found in [1] and [2].

### C. Colon structure and its optical properties

#### 1) Normal colon

The wall of the colon has four distinct layers. Starting from

the lumen these are the mucosa, the submucosa, the muscularis externa and the serosa [20]. The layers differ in their architecture, cellular properties and vascularisation which, in turn, affect their optical properties. Absorption in each layer depends mainly on its haemoglobins contents. Scatter originates mainly from collagen fibers and subcellular organelles [6] and is a function of the scatterer size, scatterer density and differences in the refractive index between the scatterers and their surrounding medium. As light enters the colon from the lumen it first accounts mucosa where some of it is absorbed by blood in mucosal capillaries and scattered by epithelial cells, organelles and collagen fibres and fibrils. The scattering within the mucosal layer and the backscatter at the boundary between mucosa and submucosa due to difference in the refractive indexes contribute to the portion of light that is re-emitted, to be subsequently measured. The remaining light enters submucosa to be absorbed by blood present in large submucosal vessels and strongly scattered forward by large collagen bundles towards the muscle layer. Some light is returned to the surface from these last two layers but because it is spatially diffused through scattering it is assumed to make a constant “background” contribution to the measured spectra. The most information is contained in the light from the mucosa layer [7].

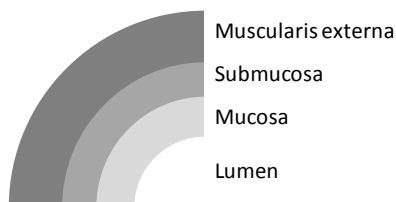


Fig. 1. The main layers of the colon. Starting from the inside of the colon (lumen) and progressing towards the outer surface of the colon are: mucosa, submucosa muscularis externa and serosa (not shown).

## 2) Colon cancer Adenocarcinoma

Adenocarcinoma is the most common type of colon cancer. As is the case with many cancers it originates in epithelial tissue, causing initially pre-cancerous changes in the mucosa. These include an increase in volume, density and disorganisation of blood microvessels, alterations in blood oxygen saturation, enlargement of cell sizes and changes in the size of collagen fibres and their density. The increase in the volume of blood is most common at the tumour periphery whereas some late cancers may show loss of microvessels in the centre leading to necrosis. Some polyps have potential to develop into cancers; they are referred to as neoplastic. Hyperplastic polyps are considered benign (in [21] Ch. 17).

## D. Overview of the method

Pixel-wise estimates of the mucosal blood volume fraction, density of the scattering particles and thickness, are derived from multispectral images of the colon using a two-stage method which extends an approach used by Claridge *et al.* [7] to quantify the mucosal blood volume fraction. In the first

(forward) stage diffuse reflectance spectra corresponding to given instances of the parameter values are computed using Monte Carlo simulation [22] [23]. This process establishes a cross-reference between the parameter values and their corresponding spectra. The second (inversion) stage determines values of the histological parameters at each point by finding parameters corresponding to the model spectrum with the best match to a measured spectrum. Spatial regularisation is simultaneously employed to maximise smoothness of the parametric maps.

## II. FORWARD MODEL

The forward model used in this work has been developed by Hidović-Rowe & Claridge and its development and validation are described fully in [6]. This section provides details essential for understanding of the inversion method and the subsequent analysis of the *ex vivo* colon data. In what follows the terms “image spectra”, “image values” and “image vectors” are used interchangeably.

The gross structure of the colon is represented by three layers: mucosa, submucosa and smooth muscle. Each layer is characterised by five histology-related parameters: blood volume fraction, haemoglobin saturation, size of scattering particles, volume fraction (density) of scattering particles and layer thickness. The plausible range of each histological parameter or (if a constant) a median value is established. Wavelength-dependent absorption and scattering coefficients are treated as constants.

A given *specific* instance of tissue can be defined by an N-dimensional parameter vector  $\mathbf{p} = [p_1 \dots p_N]$ . If the range of a parameter  $p_n$  is discretised to  $k_n$  levels, a set  $\mathcal{P}$  of  $K = k_1 \cdot k_2 \cdot \dots \cdot k_N$  parameter vectors spans a space of all the discrete instances of the colon tissue according to the plausible parameter ranges (see Table 1). Each parameter vector  $\mathbf{p}$  is then associated with an M-dimensional multispectral image vector  $\mathbf{i} = [i_1 \dots i_M]$  in a two-stage process. First, a spectrum  $\Lambda_{\mathbf{p}}$  corresponding to a given  $\mathbf{p}$  is computed by Monte Carlo simulation of photon propagation through a tissue [22]. In this method a photon with a given energy (wavelength) undergoes multiple interactions dictated by the absorption coefficient, the scattering coefficient and the scattering phase function of a given tissue layer. The interaction events decrease photon energy and alter its trajectory according to probability distributions based on photon transport theory. The photon terminates when either its energy is exhausted or when it exits the tissue. Cumulative statistics over a large number (of the order of hundreds of thousands) of photons give tissue reflectance as a ratio of the incident and re-emitted photons. To obtain the multispectral image values corresponding to tissue parameters the computed spectra are then convolved with the appropriate bandpass filters,  $F_m$ ,  $m=1, \dots, M$ , giving a set  $\mathcal{I}$  of M-dimensional image vectors  $\mathbf{i} = [i_1 \dots i_M]$ . The mapping function  $f: \mathcal{P} \rightarrow \mathcal{I}$  associating tissue parameters with their multispectral image values defines a forward model of tissue reflectance,  $\mathcal{M}$ .

The analysis of the variability of spectral reflectance as a function of the variations of the parameter values showed that only three parameters characterising the mucosa had significant effect on the spectra: blood volume fraction (BVF), density of the scattering particles (DSP) and thickness (DMUC) (see Fig. 2 adapted from [6]). The remaining parameters were shown to make constant contributions to spectral reflectance and have been set in the model to the median of their respective ranges (see Table 1).

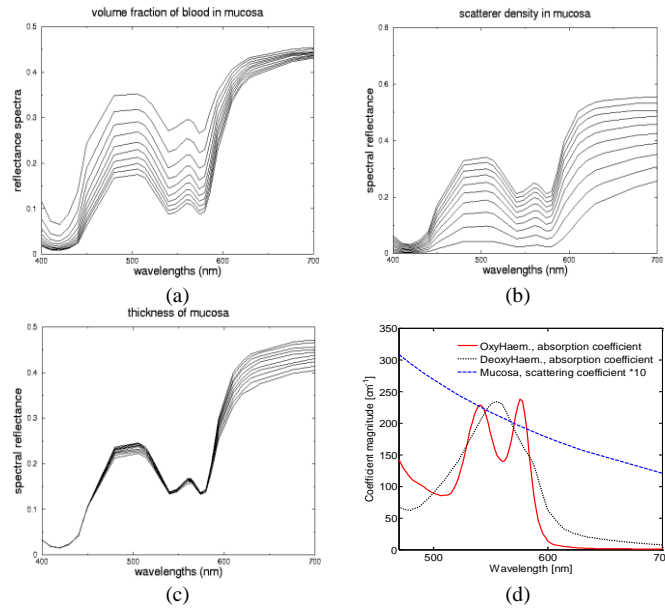


Fig. 2: (a) - (c): Variability of the spectral reflectance of the colon as a function of varying individual parameters. In each plot one parameter is varied whereas the remaining three are set to the mean values of their respective ranges. The x-axis shows the wavelength in nm and the y-axis shows the diffuse reflectance as a proportion of the incident light. (d) Absorption and scattering coefficients of the key optical constituents of the colon.

TABLE I  
HISTOLOGICAL PARAMETERS CHARACTERISING COLON LAYERS.

Parameter	Mucosa	Submucosa	Muscle
Layer thickness [μm]	250 - 735	500	900
Blood volume fraction [%]	0 - 10	10	4.5
Haemoglobin saturation [%]	70	70	85
Volume fraction of scattering particles [%]	4 - 60	30	see (*)
Size of scattering particles [μm]	0.4	2	see (*)

(\*) Scattering coefficients were obtained directly from measured data [6].

In addition to the parameters characterizing colon histology, MC simulation requires that the following parameters related to optical properties of tissues are provided: wavelength-dependent absorption coefficient for haemoglobin and oxyhaemoglobin; and for each layer the wavelength-dependent scattering coefficient, anisotropy factor, and refractive index of the medium and the scattering particles. Reference [6] gives full details of all the parameters, their sources and validation.

For the model used in this work parameter vectors  $\mathbf{p}$  characterising the tissue were constructed for the three variable parameters: BVF, DSP and DMUC. Each parameter was discretised to five levels within the range thus defining a model with  $K=3^5=125$  different instances of the colon tissue. Image vectors were computed for  $M=12$  wavelengths in the visible range. The model spectra were obtained by MC simulation, each computed using 200,000 photons.

### III. INVERSION

The forward model  $\mathcal{M}$  described above provides mapping  $f: \mathcal{P} \rightarrow \mathcal{I}$  from the space of histological parameters to the space of their multispectral image values. The inverse mapping from image values to histological properties,  $f^{-1}: \mathcal{I} \rightarrow \mathcal{P}$ , applied to real image data will generate parametric maps which show relative magnitude of the histological parameters at each pixel of the original image.

#### A. Mathematical formulation

Given a vector of measured multispectral image values at a spatial location  $(x,y)$ ,  $\mathbf{i}_{(x,y)}$ , the inversion is defined as a function  $\mathbf{p} = f^{-1}(\mathbf{i})$  such that  $\mathbf{i} = f(\mathbf{p})$ . However, since the forward model is implemented using a probabilistic Monte Carlo method, the functional form of the mapping  $f$  does not exist; hence neither does the functional form of  $f^{-1}$ . Inversion has to take a form of an estimation that, in a generic form, can be defined as finding at each image location  $(x,y)$  a parameter vector  $\hat{\mathbf{p}}$  such that

$$\hat{\mathbf{p}} = \underset{\{\mathbf{p}_i\} \in \mathcal{M}}{\operatorname{argmin}} \|f(\mathbf{p}) - \mathbf{i}_{(x,y)}\| \quad (1)$$

$\|\cdot\|$  is a distance between two spectra in an appropriate metric.

#### B. The non-uniqueness problem

When considering inversion it is important to establish whether the mapping between the parameter vectors and the image vectors is one-to-one, i.e. that the function  $f$  is bijective [24]. In the context of this work no two tissue samples characterised by different structural and optical properties should give rise to the same spectrum. If this condition is not met the accurate recovery of parameter values from the optical signal cannot be ensured. Exhaustive numerical testing was carried out on all the pairs of image vectors generated by the model,  $(\{\mathbf{i}_i\}, \{\mathbf{j}_j\}) \in \mathcal{M}$   $\mathbf{i}_i \neq \mathbf{j}_j$ . To account for the effects of the imaging system the model outputs were convolved with the imaging system response functions. Given the stochastic nature of MC the modelled spectra have an associated error  $\varepsilon_{MC}$ . Therefore two spectra were considered the same if the distance  $\|\cdot\|$  between them was smaller than the error  $\varepsilon_{MC}$  ( $=0.034$ ) estimated for the MC using 100,000 photons. This analysis identified that approximately 10% of image vector pairs with significantly different parameter vectors have



spectra differing by less than  $\epsilon_{MC}$ . This demonstrated that a solution to the model inversion problem using a simple inverse mapping scheme, such as successfully employed e.g. by [4], is ill-posed.

### C. Optimisation using spatial regularisation

A simple minimisation in equation (1) generates solutions independently for each pixel. The instability of this estimation can be demonstrated by inspecting a typical solution space for a sample pixel (Fig. 3). There are five potential candidates for global minima for which  $\|f(\mathbf{p}) - \mathbf{i}_{(x,y)}\|$  is below the stochastic error  $\epsilon_{MC}$  in the MC model.

Assuming that the spatial variations in the values of histological parameters are fairly smooth a better estimate  $\mathbf{p}$  can be found by imposing a spatial smoothness criterion on a set of candidate solutions. This can be achieved by an optimisation scheme that minimises local discrepancies in the parameter space  $\mathcal{P}$  whilst maintaining spectral error as low as possible:

$$\tilde{\mathbf{p}} = \underset{\{\mathbf{p}, \mathbf{i}\} \in \mathcal{M}}{\operatorname{argmin}} \|f(\hat{\mathbf{p}}) - \mathbf{i}_{(x,y)}\| + \beta \|f^{-1}(\mathbf{i}_{(x,y)}) - f^{-1}(\mathbf{i}_{(x',y')})\| \quad (2)$$

where  $\hat{\mathbf{p}} = f^{-1}(\mathbf{i})$  is a current estimate (e.g. an initial estimate obtained according to the equation (1)),  $\mathbf{p}' = (x', y')$  represents a neighbourhood of image pixel at  $(x, y)$ ,  $\beta$  is a regularisation parameter and  $\|\cdot\|$  is a distance function. For simplicity the equation (2) can be written in a canonical form as

$$\tilde{\mathbf{p}} = \underset{\{\mathbf{p}, \mathbf{i}\} \in \mathcal{M}}{\operatorname{argmin}} V_d(f(\hat{\mathbf{p}}), \mathbf{i}) + \beta V_s(\hat{\mathbf{p}}, \mathbf{p}') \quad (3)$$

where data term  $V_d$  accounts for discrepancy between the image and the model spectrum and smoothness term  $V_s$  penalises for discrepancy between the neighbouring parameter values at each image point.

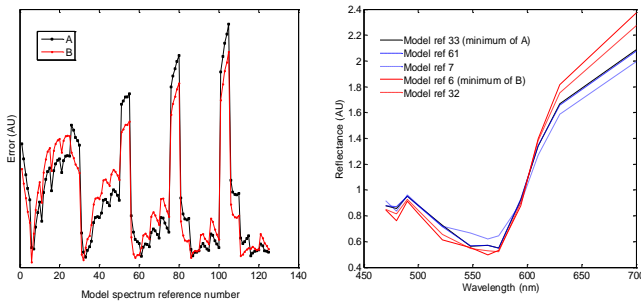


Fig. 3. Left: a typical solution space for two neighbouring pixels, A and B over  $K(=125)$  model entries. Pixel A has minimum for the model spectrum reference number 33, pixel B for number 6. Their parameter vectors [BVF DSP DMUC] are A: [0.025 0.05 400] and B: [0.005 0.05 200]. Normalised distance in parameter space between A and B is 0.389. After optimisation pixel B solution was reassigned to the model reference number 32, parameter vector [0.025 0.05 300], decreasing the distance in parameter space to 0.167 whilst increasing spectral matching error by 2%. Right: model spectra corresponding to several local minima in the solution space for pixels A & B.

### D. Implementation of the model inversion

The inversion was implemented as a Discrete Markov Random Field (DMRF) optimisation using an Iterated Conditional Modes (ICM) algorithm [25]. Briefly, a MRF represents a joint probability distribution in the form of a graph [26, 27]. Graph nodes represent observed quantities (random variables  $Y_i$ ) determined by hidden properties (variables  $X_i$ ) of the related Markov Random Field. A set of random variables is said to form a Markov Random Field if probabilities  $p(X_i)$  are strictly positive and if the properties of any node in the graph depend only on the properties of its immediate neighbours. In a DMRF  $X_i$ -s assume discrete values, also known as labels. In this work nodes of the graph correspond to image points, edges represent probabilistic dependencies between the nodes, the observed quantities are image vectors  $\mathbf{i}$ , and hidden properties are tissue properties represented by parameter vectors  $\mathbf{p}$ . The objective of optimization is to assign a label  $\mathbf{p}$  to each of the observed quantities (an image vector  $\mathbf{i}$ ) such that an objective function of the form given by equation (3) is minimised. In the context of MRF-s  $V_d$  is referred to as the data term and  $V_s$  as the prior term.

The ICM algorithm iteratively maximises the probability of each variable in the MRF conditioned on its neighbours. This algorithm was chosen for its appropriateness for the inversion problem in hand and simplicity of implementation whilst providing adequate speed of execution (approximately 1 minute for 518x680x12 spectral image dataset using Matlab R2009a on a PC Intel® Core™ Quad, 2.33GHz, 4 GB memory). The development of optimisation techniques for MRF-s is an active research field and algorithms involving methods such as graph-cuts, message passing and higher order potentials [28] [29] [30] [31] provide much more powerful solutions than the traditional ICM algorithm used here. Their use will be considered in future implementations.

#### Algorithm: ICM

```

1:  $k \leftarrow 0$ 
    $\mathbf{i} \leftarrow$  initialise
    $\mathbf{p}^{(k)} \leftarrow$  initialise
    $V \leftarrow \max(\|\mathcal{M}(\mathbf{p}_m), \mathcal{M}(\mathbf{p}_n)\|_2) + 4 * \beta * \max(\|\mathbf{i}_m, \mathbf{i}_n\|_1)$ 
2: do
3:   for each  $\mathbf{p}$  represented in  $\mathcal{M}$  do
4:      $V_d \leftarrow \|\mathcal{M}(\mathbf{p}) - \mathbf{i}\|_2$ 
5:      $V_s \leftarrow \min(VN(\mathbf{p}^{(k)}, \text{neighb } \mathbf{p}^{(k)}), \text{max\_dist})$ 
6:      $V^{(k)} = V_d + V_s$ 
7:     if  $V < V^{(k)}$ 
        $\mathbf{p}^{(k)} \leftarrow \mathbf{p}$ 
        $V \leftarrow V^{(k)}$ 
     endif
8:   endfor
9:    $k = k + 1$ 
10: while  $(V^{(k)} - V^{(k-1)}) > \text{eps}$ 

```

In the above  $\mathcal{M}(\mathbf{p}_i)$  is a model spectrum corresponding to parameter  $\mathbf{p}_m$ ,  $\max(\|\mathcal{M}(\mathbf{p}_m), \mathcal{M}(\mathbf{p}_n)\|_2)$  and  $\max(\|\mathbf{i}_m, \mathbf{i}_n\|_1)$  are maximum distances in the model  $\mathcal{M}$  and in the image data respectively;  $\|\cdot\|_n$  is metric  $L^n$ ;  $\max\_dist$  is a constant limiting the distance in the parameter space;  $VN(\cdot)$  is a function that computes a value of the smoothness term for  $\mathbf{p}$  and its immediate four neighbours  $\mathbf{p}'$ :

$$VN(\mathbf{p}, \mathbf{p}') = \sum_{\mathbf{p}'} \|\mathbf{p} - \mathbf{p}'\|_1 \cdot \mathcal{L}(\mathbf{p} | \text{neighb } \mathbf{p}') \quad (4)$$

where  $\mathcal{L}$  is a function expressing the likelihood of  $\mathbf{p}_m$  and  $\mathbf{p}_n$  having the matching spectra,  $\mathcal{L}(\mathbf{p}_m, \mathbf{p}_n) = e^{-\|\mathcal{M}(\mathbf{p}_m), \mathcal{M}(\mathbf{p}_n)\|_2}$ .

One of the known drawbacks of the ICM algorithm is its sensitivity to intialisation. This problem was addressed here by making an explicit use of the forward model  $\mathcal{M}$ . As described in section II, the model comprises 125 pairs  $\{\mathbf{p}, \mathbf{i}\} \in \mathcal{M}$  of parameters  $\mathbf{p}$  and their paired image vectors  $\mathbf{i}$ . For a given measured  $\mathbf{i}_{(x,y)}$  (which may not belong to a set of discrete image vectors in  $\mathcal{M}$ ) its nearest neighbour in  $\mathcal{M}$  is found using  $L^1$  metric,  $\|\mathbf{i}_k - \mathbf{i}_{(x,y)}\|_1$ . Parameter vector  $\mathbf{p}_k$  corresponding to the image vector  $\mathbf{i}_k$  is used as an initial value.

Fig. 3 illustrates the effects of the optimisation. The parameter vector  $\hat{\mathbf{p}}$  representing the best spectral match for image vector  $\mathbf{i}_{(x,y)}$  at pixel B is at relatively large distance from another pixel in its local neighbourhood. After the optimisation stage the parameter values ascribed to  $\mathbf{i}_{(x,y)}$  become close to those of its neighbours according to term  $V_s$  in equation (3) whilst the distance between the spectrum corresponding to  $\hat{\mathbf{p}}$  and the spectrum at  $(x,y)$  (term  $V_d$ ) increases only slightly (see caption in Fig. 3).

#### E. Validation of model inversion

The ability of the inversion to recover correct parameter values from the image spectra was tested on computer-generated data. The input was in the form of 80x80 parametric maps formed of nine regions of different tissue type. Each region was assigned known levels of blood volume fraction, density of scattering particles and thickness of mucosa with values chosen to mimic normal tissues (N1 - N3), adenocarcinomas at different stages (C1 - C4), necrotic tissue (NE) and blood pockets (BP) that were frequently present in the folds of the *ex vivo* samples. The maps were contaminated with Gaussian noise to match the mean SNR of the real image data of 18 dB (range 11 - 24 dB). Their image vectors were generated using Monte Carlo simulation with 100,000 photons. The resulting multispectral-like image containing 400 spectra was used to test the ability of the inversion to recover parameter values from image spectra. Since no assumptions could be made about statistical distribution of data non-parametric tests were employed. Normalized root-mean-square deviation (NRMSD) was computed to measure discrepancies in between the input and the recovered parameter values. Spearman's rank correlation coefficient ( $\rho$ ) measured dependence between input and output data.

The results of inversion depended on the value of the regularization parameter  $\beta$  which dictated the balance of penalty between the data term  $V_d$  and the smoothness term  $V_s$ . Increasing  $\beta$  resulted in spatially smoother but spectrally less accurate reconstructions. Plots in Fig. 5 illustrate the effects of varying  $\beta$  on Spearman's  $\rho$  and NRMSD. The optimal performance (at maximum of  $\rho$  and minimum of NRMSD) occurred at value of  $\beta = 0.1$  with  $\rho = 0.80, 0.82, 0.34$  and  $\text{NRMSD} = 1.78, 1.80, 2.54$  in the reconstruction of blood volume fraction (BVF), density of scattering particles (DSP) and thickness of the mucosa (DMUC) respectively. Fig. 4 shows the labelled input data and the resulting recovered parameter maps. The results are consistent with the variation of spectra magnitudes as a function of parameter values (see Fig. 2). Where these variations are large, as for BVF and DSP, a change in the parameter value results in a discernible change in spectral reflectance. Where spectral reflectance does not change much, as for DMUC, inversion in the presence of error is less reliable. The overall mean value of  $\rho = 0.653$  indicates moderately strong and statically significant ( $p < 0.0001$ ) correlation between input and output parameters in the presence of noise. The BVF parameter shows fairly strong degree of correlation ( $\rho = 0.80$ ) which is important in this study as the increase in the volume of blood is a significant feature of adenomatous lesions. Plots in Fig. 6 provide a further insight into the quality of inversion. Although there is a significant spread around the mean of the recovered parameter values, the relationship between the input and the output parameters is monotonic. This means that the inversion cannot be relied upon to return quantitative results; however, it can show relative variations in the parameter values.

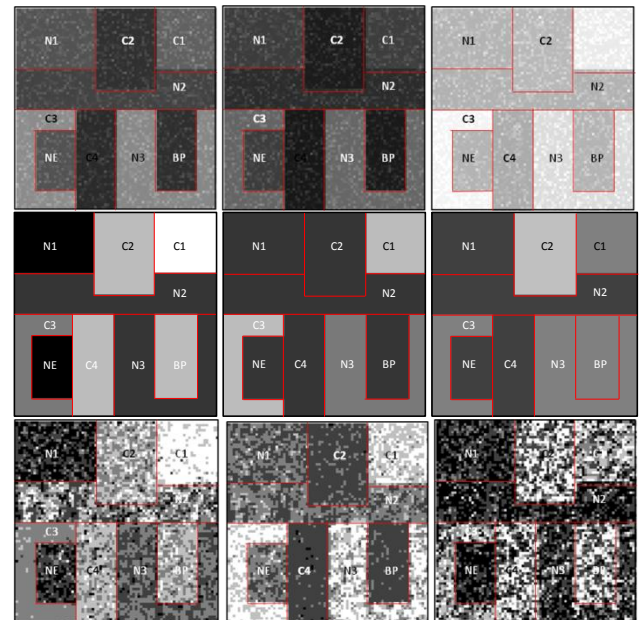


Fig. 4. Simulated parametric maps and the recovered parameters. Top: Samples of input images contaminated with noise at 470, 548 and 700nm. Middle and bottom: input parameters; and parameters recovered from the noisy map maps of (from left to right): blood volume fraction (BVF); density of scattering particles (DSP); thickness of mucosa (DMUC).

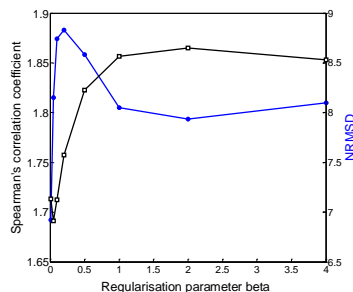


Fig. 5. Spearman's rank correlation coefficient and normalized root-mean-square deviation as a function of the regularization parameter.

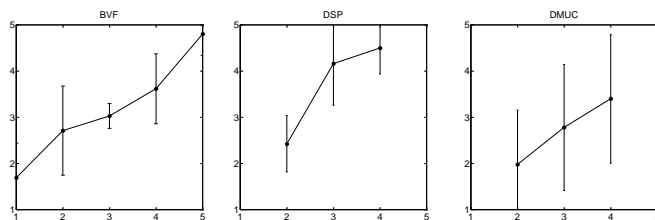


Fig. 6. Parameter recovery; comparison of the noise-free input data (x-axis) and the recovered data (y-axis) using MRF-ICM with  $\beta = 0.1$ .

#### IV. EXPERIMENTS ON EX VIVO TISSUE SAMPLES

##### A. Subjects, materials and procedures

*Ex vivo* colon samples used for imaging were obtained during ordinary surgical procedures performed at the Queen Elizabeth Hospital in Birmingham (QEH), UK. Patients were considered suitable for inclusion if diagnosed as abnormal, i.e. having colon cancer or large adenomatous polyps at the preoperative screening for colon cancer; and if they gave informed consent for using their tissue samples for research purposes. Patients were randomly selected, with no preference for age, gender or previous medical history. Table 6 provides information on the eight patients included in the study.

##### B. Sample preparation

According to the surgical protocol at QEH all the samples excised from the body comprised the primary tumorous site, and where possible at least two centimetres of the surrounding tissue. The excised samples were cut open and any traces of faeces washed out. The samples were then pinned down flat onto a black surface. Flattened samples were placed in formalin, an optically neutral fixative. Images were acquired within two hours of tissue extraction. Immediately prior to imaging the samples were removed from the formalin and placed at the sample port of the integrating sphere. After imaging the samples were placed back in the formalin and taken for histological analysis to the Department of Pathology at the University of Birmingham where they underwent routine microscopic examination. The findings of the histological analysis were then used as the "gold standard" to verify the results of computer analysis. The computer analysis was blind to histology results.

##### C. Imaging system

The imaging system comprised a light source (30 cm diameter integrating sphere with a halogen-tungsten satellite sphere illuminator SSI-030, Prolite, U.K.), liquid crystal tunable filters (VariSpec<sup>TM</sup>, CRI, U.S.A.) and a 12 bit monochrome camera (Retiga<sup>TM</sup> EXi Fast 1394, Imaging, Canada). The integrating sphere was used to ensure a uniform and diffuse illumination across the whole imaged area of the sample. Samples were placed at a 7.5 cm sample port of the integrating sphere. The VariSpec filters were mounted in front of the camera lens and positioned at the camera port of the sphere. Both the camera and the filters were controlled by a custom-written software that allowed the selection of the filter's central wavelength and the camera's exposure time, gain, offset and binning. It also ensured synchronisation of the camera shutter with the filter changes. All the components of the imaging system were spectrally calibrated. The schematic drawing of the imaging system can be found in [36] Fig. 3.

##### D. Image acquisition

Images of tissue samples were acquired at 31 wavelengths between 470nm and 700nm. The exposure times ranged from 0.07 to 0.009 seconds. The total acquisition time was less than 10 seconds. All the other camera acquisition parameters (gain=1, offset=0 and binning=2) were constant for all the wavelengths and all the samples.

##### E. Normalisation

Normalisation consists of two steps: (1) removing the effects of the imaging system and (2) compensating for geometry-related changes in image brightness. Step 1 is necessary to obtain correct spectral information and is applied only to real image data. Step 2 makes it possible to compare spectral shapes regardless of their magnitude.

Spectral characteristics of the imaging system were obtained by acquiring images of the Spectralon<sup>TM</sup> 50% reflectance standard (Labsphere) immediately after imaging of the tissue and under the same imaging conditions. Dividing a tissue spectrum by a Spectralon spectrum and the exposure time removed the imaging system dependent factors including acquisition time, filter transmittance, camera quantum efficiency and camera gain, all wavelength dependent [32].

The surface of a normal colon has numerous folds and surface areas of the cancer are typically raised or depressed with respect to the surrounding tissue. A further normalisation had to be applied to compensate for difference in the intensity of light recorded by the camera as a function of tissue geometry. As the light intensity changes as a function of the distance and the angle between a surface and a detector, two image spectra  $s_1$  and  $s_2$  of the same point  $s$  acquired at two different distances  $d_1$  and  $d_2$  and / or inclinations  $a_1$   $a_2$  will have the same shape but will vary by a constant; i.e. for each wavelength  $\lambda$   $s_1(\lambda)=s(\lambda)a_1/d_1^2$ ,  $s_2(\lambda)=s(\lambda)a_2/d_2^2$ . Integrating the spectra across the wavelength range yields two constants that differ only by a distance and an inclination related



factors. By dividing an individual spectrum by a constant  $c_{IN}$  equal to its integral with respect to  $\lambda$  (equivalent to total remittance at a given range of  $\lambda$ ) removes the distance and angular dependence as well as dependence on an overall magnitude of the spectrum. Spectra normalised in this way represent *variations* in spectral reflectance as a function of wavelength. Similar normalisation is applied also to the model spectra so that image spectra can be compared to the model spectra in a meaningful way. Normalising constants  $c_{IN}$  are stored for each image point to be used in validation (section IV.G).

#### F. Inversion

The normalised spectral data was processed to generate parametric maps by applying the inversion algorithm DMRF-ICM described in section III.B with parameters that were found to yield best results on simulated data (section III.E). Three parametric maps were generated showing variability of mucosal parameters across the sample: blood volume fraction (BVF), density of scattering particles (DSP) and thickness (DMUC). In addition to these histologically-related maps the error map was constructed. It depicts the magnitude of discrepancy between the measured spectrum and the corresponding model spectrum (equation (1)). The error was typically larger in areas of cancer and abnormal (e.g. necrotic) tissue than in areas of normal tissue. It was also larger in the areas of the large tissue curvature and of the sudden changes in tissue structure. The elevated error values suggested that the model does not contain spectra representative of the tissue at a given point. As one reason for a large error is the presence of an unknown abnormality, implicitly such map may depict “suspicious” tissue regions.

#### G. Validation

As with most *in vivo* measurements of human tissues absolute validation is problematic because of unavailability of ground truth data related to important parameters such as for example blood concentration. Validation of the forward model in [6] confirmed its ability to generate spectra that could be fitted to the measured colon spectra. Evaluation of the inversion on the computer generated data in III.E showed that the parametric maps correspond to magnitudes of the blood volume fraction and density of scattering particles with fair statistical accuracy, and the thickness of mucosa with moderate statistical accuracy. Repeatability of the parameter recovery is examined in sub-section 1) and the reconstruction error is discussed in sub-section 2).

##### 1) Repeatability

To test the repeatability of the inversion the parametric maps of two sets of images of the same tissue sample were registered using Matlab functions (`cpselect`, `cp2tform`, `imtransform`) and the values in the overlapping regions compared for each map. Mean percentage differences were 17.2% for BVF map, 9.3% for DSP map and 11.7% for the DMUC map. Normalised root-mean-square deviation

(NRMSD) values of 1.29 (BVF), 1.17 (DSP) and 2.34 (DMUC) were in line with the parameter recovery errors for the simulated data (III.E).

##### 2) Spectral correspondence of reconstructions

If parameters obtained by inversion are correct, the multispectral image data reconstructed by the application of the forward model to the parameter vectors should result in images that closely resemble the originals, i.e.  $f(\hat{\mathbf{p}}) = \mathbf{i} + \boldsymbol{\varepsilon}$ . Reconstructions are computed as follows. At each image point inversion results in a parameter vector  $\hat{\mathbf{p}}$ . A corresponding (normalised) spectrum  $\mathcal{M}(\hat{\mathbf{p}})$  is retrieved from the model and multiplied by a normalization constant  $c_{IN}$  (section IV.E), yielding the spectral shape representative of  $\hat{\mathbf{p}}$  and with the brightness magnitude of the original image. Fig. 7 shows examples of the original images  $\mathbf{i}$  and their reconstructions  $f(\hat{\mathbf{p}})$  at several wavelengths.

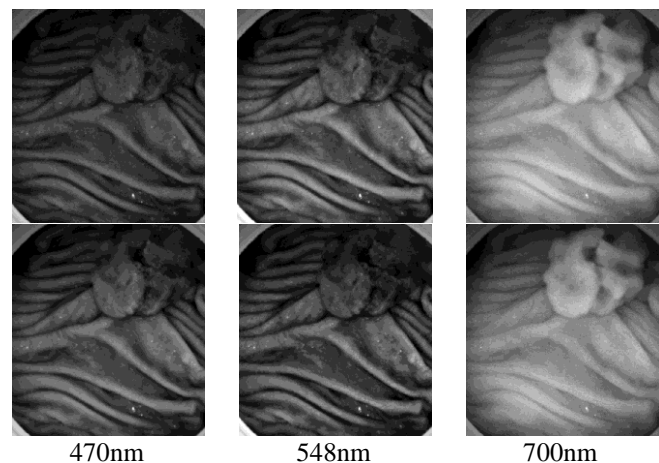


Fig. 7. Examples of the originals and their reconstructions. Top row: original images. Bottom row: images reconstructed from the parametric maps.

## V. RESULTS AND THEIR ANALYSIS

### A. Qualitative observations

Prior to quantitative analysis in section V.B initial validation was carried out on image data, spectral data and parametric maps to verify whether their gross appearance is in line with the expectations based on tissue physiology.

#### 1) Multispectral image data

Fig. 7 shows a set of images at wavelengths 470nm, 548nm and 700nm of a tissue sample containing adenocarcinoma together with a wide margin of a healthy tissue. Blood vessels and smaller features of the tissue can be seen in the mid green region (548nm) where blood absorption is strong. In the blue region (470nm) the features are less distinct because high blood absorption coefficient causes even small amounts of blood to absorb strongly thus reducing differentiation between high and low blood levels. In deep red (700nm) those features disappear because of small absorption of light by haemoglobin derivatives present in the blood.

#### 2) Image spectra

Spectra in Fig. 8, left, show features characteristic of absorption by haemoglobins indicating that the imaged



excised tissue samples were not completely deprived of blood. For instance in the plot for the on-vein spectrum, where blood absorption is strong, spectral reflectance shows a dip in spectral reflectance at around 540 - 580 nm which coincides with peaks in the haemoglobins' absorption spectra (see Fig. 2(d)). The same spectral behaviour can be observed on the right-hand side graph in Fig. 8 showing modelled spectra generated with lower (dashed line), and higher (solid line) blood content. The overall reflectance is lower for an on-vessel point indicating stronger absorption.

A comparison of the spectra of cancerous and normal tissue can be seen in Fig. 9. The graph on the left shows measured spectra. The main spectral variations seem to be due to higher blood content of the cancerous polyp and higher thickness of the mucosa: higher blood volume fraction results in stronger absorption of light in the spectral range c. 400-600nm where the absorption coefficient for haemoglobins is higher and therefore the reflectance is lower; higher thickness results in stronger scatter (reflectance is higher in the red end of the spectrum, 600-700nm). The changes in these spectra are consistent with known histological variations which occur with development of malignancy [33] (see section I.C.2). Analogous spectral variations are reproduced by the model (Fig. 9, right).

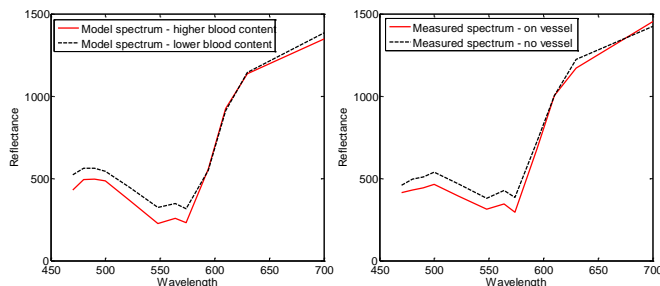


Fig. 8. Spectra of normal colon tissue. Left: measured spectra; red solid line is a spectrum of tissue with visible blood vessels; black dashed line is a spectrum of tissue with no visible blood vessels. Right: the analogous spectral behaviour of the modelled spectra achieved by increasing the blood volume fraction value. The corresponding parameter vectors [BVF DSP DMUC] are: on-vessel [0.1 0.1 400], away from a vessel [0.025 0.05 400].

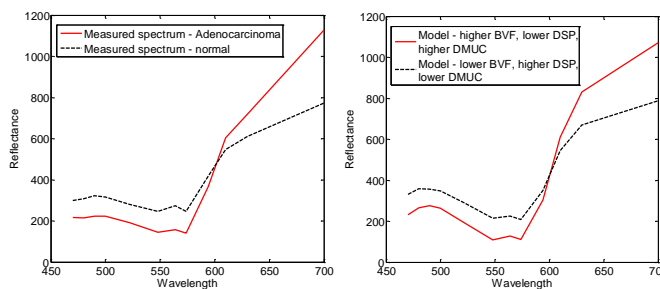


Fig. 9. Comparison of spectra of normal and cancerous colon tissue. Left: measured spectra; red solid line is a spectrum of histologically proven adenocarcinoma; black dashed line corresponds to normal tissue. Right: analogous spectral differences visible in the modelled spectra. The corresponding parameter vectors [BVF DSP DMUC] are: adenocarcinoma [0.1 0.05 500], normal tissue [0.025 0.05 400].

### 3) Parametric maps

As an example Fig. 10A shows the RGB image, the three histological parametric maps and the error map for a sample containing adenocarcinoma. Other cases, classified under five histological class headings, are discussed in section V.B below. In all the parametric maps darker and lighter pixels represent respectively smaller and larger amounts of the corresponding histological parameter. The white and red spots 3 mm in diameter are pins. The polypoid lesion in Fig. 10A delineated with a white line on the RGB image was histologically diagnosed as an adenocarcinoma. The parametric maps show that in comparison to the normal tissue the cancerous site has increased blood volume fraction in mucosa, decreased scattering density and increased mucosal thickness. The error map shows an increase in the error between modelled and measured spectra in a small region within the cancerous tissue. Given that the error is not very large, the parameter values extracted can be assumed to be representing the structure of the cancer reasonably well. The rest of the tissue appears to be fairly uniform in terms of parameter values, except for the folds on the tissue surface. The valley of a large fold in the periphery has an increased error because it was not adequately illuminated. Some folds contain residual pockets of blood accumulated there after the sample was excised and mounted, and appropriately show high blood volume contents in the parametric map of the blood volume fraction.

### B. Quantitative analysis of parametric maps

To investigate whether parametric maps show quantitative differences in relation to different pathologies, the tissue samples were assigned to five histological classes: normal tissue, adenocarcinoma, adenocarcinoma with necrosis, neoplastic polyps and hyperplastic polyps. All cancers were histologically proven adenocarcinomas at different stages of development and penetration into the colon wall. To investigate whether the parametric maps show differences between various tissue types a set of points was randomly selected from the histologically confirmed primary cancerous tissue and from the normal tissue more than 2 cm away from the primary tumour site.

In each sample 1000 points were used per tissue type unless the respective area was smaller in which case all the points were used. A Kruskal-Wallis test was performed to establish whether the groups of data belonging to different types were significantly different. If they were, a Mann-Whitney test with Bonferroni correction was applied in order to calculate the significance of difference between all the pairs of the data groups. The level of significance was set to 95% ( $p_1 < 0.05$ ). The tests were carried out individually for each sample. It is important to note that the key indicators of abnormality are *relative differences* in parameter values in normal and abnormal tissues. Normal tissues exhibit considerable variability and any two patients will almost certainly have different base values of the histological parameters, and

“normal” levels of one parameter in one patient might indicate abnormality in another. Tables 2-5 show the mean and standard deviation of each parameter. For all the pairwise combinations of tissue types the significance  $p_1$  is reported.

#### 1) Case 1: Adenocarcinoma

Qualitative analysis of this case was carried out as described in section A.3). Table 2 shows quantitative results of the post hoc test on the sample shown in Fig. 10A. The sample contains two tissue types: normal (N) and cancerous (C). Normal and cancerous tissue differ significantly in all parameter values. This is important as it suggests that in this sample the cancerous site is statistically different from the normal tissue.

#### 2) Case 2: Adenocarcinoma with necrotic tissue

Table 3 shows the results for the sample in Fig. 10B. The sample contains four tissue types: the central necrotic part of the cancer (CN), the cancer surrounding the necrotic area (C), tissue surrounding the cancer (S) and the polyp (P). The surrounding tissue and the necrotic cancer, as well as the surrounding tissue and non-necrotic cancer, differ significantly in all the parameters. The same is the case when the polyp's parameter values are compared to those of the two cancer regions. Those two regions differ significantly from each other in all the parameters which should be expected given that necrosis changes considerably the tissue structure. It is interesting to note that the small adenomatous polyp appears to be visible in all three parametric maps showing characteristics similar to those of the non-necrotic cancerous tissue in the left margin of the large tumour. The increased values of the blood volume fraction, collagen density and mucosal thickness are characteristic of active malignant growth. This is important as it suggests that even a very small adenomas might be detectable.

#### 3) Case 3: Neoplastic polyp

The sample shown in Fig. 10C contains two tissue types: neoplastic polyp (P) and the normal tissue (N). The results are summarised in Table 4. The polyp and the normal tissue differ significantly in all the parameters. This might suggest that the polyp might be suspicious, especially as a large error value in the error map indicates that the polyp's architecture might be different to that assumed in the model.

#### 4) Case 4: Hyperplastic polyp

Table 5 shows the results for the sample containing a hyperplastic polyp in Fig. 10D. The sample contains two tissue types: the polyp (P) and the normal tissue (N). These two tissue types differ significantly in all parameters but mucosal thickness. A similar tendency was observed for hyperplastic polyps of other tissue samples.

#### 5) Analysis of ex vivo results

In total 12 lesions from 8 *ex vivo* samples were analysed. shows the lesion type and the mean parameter values from the lesions (-L) and from the neighbouring areas of the colon (-N). A large lesion in dataset 4 has been sub-divided into two regions, the central necrosis (4.3) and the surrounding cancer (4.2).

From the tumour histology (section I.C.2) and the analysis of the tissue reflectance model the following characteristics should be expected for the cancerous lesions in comparison to the neighbouring normal tissue: increase in blood volume fraction (BVF); decrease in density of scattering particles (DSP); and change in mucosal thickness (DMUC). Of these the changes in the blood volume fraction would be a most reliable indicator because the variation of spectra magnitudes as a function of parameter values are large (Fig. 2) and its recovery by the model inversion is most accurate (section III.E).

TABLE 2  
RESULTS OF MANN-WHITNEY TEST WITH BONFERRONI CORRECTION ON THE PARAMETRIC MAPS SHOWN IN FIG. 10A.

Tissue sample		BVF	DSP	DMUC
Normal (N)	mean	0.046	0.073	318.58
	std	0.032	0.030	117.99
Cancer (C)	mean	0.071	0.079	427.66
	std	0.030	0.040	140.44
p1 (N vs C)		<0.0001	<0.0001	<0.0001

TABLE 3  
RESULTS OF MANN-WHITNEY TEST WITH BONFERRONI CORRECTION ON THE PARAMETRIC MAPS SHOWN IN FIG. 10B.

Tissue sample		BVF	DSP	DMUC
Surrounding (S)	mean	0.020	0.079	269.54
	std	0.032	0.030	117.99
Polyp (P)	mean	0.021	0.072	291.88
	std	0.019	0.026	79.56
Cancer (C)	mean	0.042	0.056	277.70
	std	0.031	0.021	85.31
Cancer, Necrosis (CN)	mean	0.017	0.051	246.21
	std	0.019	0.007	56.34
p1 (S vs P)		>0.05	>0.05	>0.05
p1 (S vs C)		<0.0001	<0.0001	<0.0001
p1 (S vs CN)		<0.0001	<0.0001	<0.0001
p1 (P vs C)		<0.0001	<0.0001	0.0004
p1 (P vs CN)		<0.0001	<0.0001	<0.0001
p1 (C vs CN)		<0.0001	<0.0001	0.0002

TABLE 4  
RESULTS OF MANN-WHITNEY TEST WITH BONFERRONI CORRECTION ON THE PARAMETRIC MAPS SHOWN IN FIG. 10C.

Tissue sample		BVF	DSP	DMUC	BVF
Normal (N)	mean	0.031	0.054	251.30	0.0590
	std	0.026	0.013	68.89	0.0090
Polyp (P)	mean	0.098	0.050	332.27	0.1400
	std	0.008	0.004	93.98	0.0234
p1 (P vs N)		<0.0001	<0.0001	<0.0001	<0.0001

TABLE 5  
RESULTS OF MANN-WHITNEY TEST WITH BONFERRONI CORRECTION ON THE PARAMETRIC MAPS SHOWN IN FIG. 10D.

Tissue sample		BVF	DSP	DMUC	BVF
Normal (N)	mean	0.023	0.057	250.67	0.023
	std	0.018	0.018	60.93	0.018
Polyp (P)	mean	0.018	0.050	253.73	0.018
	std	0.010	0.000	59.42	0.010
p1 (N vs P)		0.0328	<0.0001	>0.05	0.0106

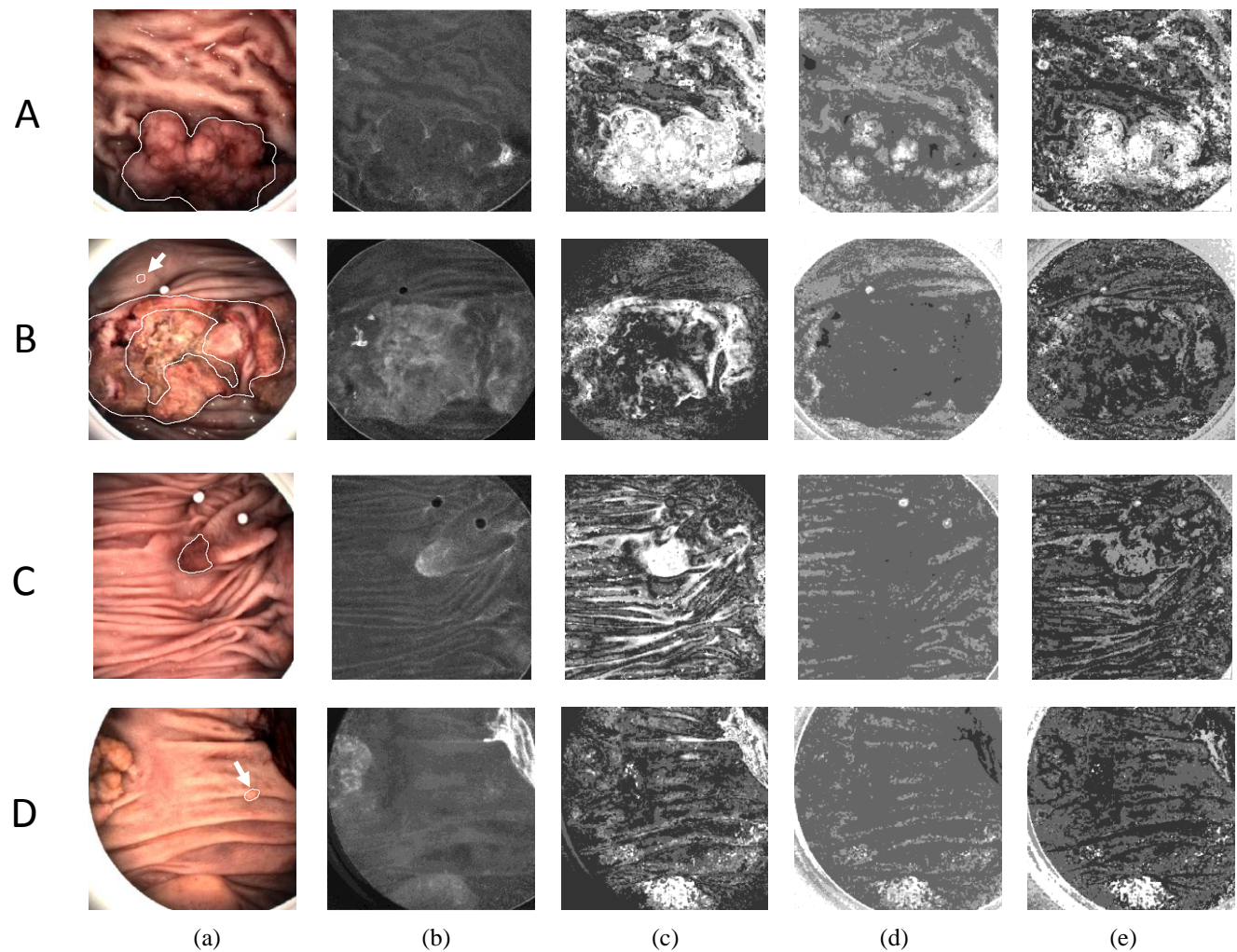


Fig. 10. From top to bottom, sample containing: (A) adenocarcinoma, (B) adenocarcinoma with necrotic tissue and an adenomatous polyp (arrow), (C) neoplastic polyp, and (D) hyperplastic polyp (arrow). Columns show: (a) RGB image, (b) error map, (c) blood volume fraction (BVF), (d) density of scattering particles (DSP), and (e) thickness (DMUC).

TABLE 6  
COMPARISON OF THE MEAN PARAMETER VALUES FROM THE LESIONS AND FROM THE NEIGHBOURING AREAS OF THE COLON.

Subject	Gender	Age	Lesiontype (stage)	Set	BVF-L	DSP-L	DMUC-L	BVF-N	DSP-N	DMUC-N
1	F	55	Adenocarcinoma (III)	2	0.071	0.079	427.66	0.046	0.073	318.58
2	F	80	Adenocarcinoma (I)	3	0.047	0.059	304.48	0.020	0.063	257.30
3	F	102	Adenomatouspolyp	4.1	0.021	0.072	291.88	0.020	0.079	269.54
3			Adenocarcinoma (II)	4.2	0.042	0.056	277.70	0.020	0.079	269.54
3			Adenocarcinoma (Necrosis)	4.3	0.017	0.051	246.21	0.020	0.079	269.54
4	F	103	Adenocarcinoma (I)	5	0.074	0.050	347.10	0.015	0.065	269.41
5	M	64	Adenocarcinoma (II)	6	0.067	0.100	416.48	0.019	0.074	272.33
6	F	86	Adenoma	7	0.098	0.049	323.66	0.025	0.062	256.49
6			Adenocarcinoma (I)	8	0.042	0.053	267.54	0.037	0.060	273.20
6			Adenomatouspolyp	8.1	0.073	0.050	331.64	0.037	0.06	273.2
6			Neoplastic polyp	9	0.098	0.050	332.27	0.031	0.054	251.30
7	M	48	Tubulo-VillousAdenoma	10	0.027	0.055	258.23	0.018	0.053	256.91
7	F	76	Hyperplastic polyp	11	0.018	0.050	253.73	0.023	0.057	250.67



Fig. 11 top, shows the values of BVF in a lesion plotted against the BVF difference between the lesion and the neighbouring tissue. All adenocarcinomas but one show higher absolute values and higher differences. The exception is a cancerous lesion in set 8. Other lesions with lower relative BVF values are 4.3 (necrosis, marked N), 11 (hyperplastic benign polyp, marked HP) and 10 (Tubulo-Villous Adenoma, marked TVA) which is a benign tumour with a potential to become cancerous. This is correct as necrotic and non-malignant lesions should not show elevated levels of blood volume fraction. In a plot DMUC (Fig. 11 bottom) all the lesions of grade II-III (2, 4.2 and 6) show an increased thickness of the mucosa whereas the region of necrosis (lesion 4.3) shows marked thinning. A similar plot for DSP (not shown) does not display significant trends. A plot of BVF against DSP (Fig. 12) for the lesions and neighbouring regions shows that the malignant lesions tend to have higher BVF values and lower DSP values than the neighbouring regions. Both trends are consistent with histology. Closer inspection of the distribution of BVF and DSP parameters within the cancerous regions will further increase confidence in the histological plausibility of the parametric maps. In the adenocarcinoma with necrosis (Fig. 10) there is strong increase in blood contents at the tumour margins where the tumour growth is active, but the necrosis region in the tumour centre is deprived of blood. Uneven distribution of blood can be observed in the tumour in Fig. 10A. In those (and other, not shown) tumours the peaks in BVF often coincide with the peaks in DSP. This is not necessarily evidence of a cross-talk between the two parameters. Collagen metabolism studies showed that collagen density tends to be greater in the first stages of the neoplasia and decreases during the development of the tumour [34]. Angiogenesis followed a similar pattern. Electron microscopy analysis of collagen networks in human large intestine showed that collagen density tends to be elevated in the centre of adenocarcinomas and decreases towards the periphery; and that the overall density of collagen tends to be lower in the tumour than in the surrounding tissue [35]. These patterns can be observed in the DSP maps. The variability of collagen density is therefore a possible reason why the scatterplots in Fig. 11, which show mean values within pathological regions, display less distinct trends than might be expected from visual examination of the parametric maps

#### 6) Classification based on parametric maps

Classification is often used as an endpoint of analysis to differentiate automatically between pathological and normal regions. This was not the intention of this study; classification was used simply as an analytical instrument to investigate whether pixel-wise classification based on parametric maps would confirm the trends in relationships between pathological regions and their adjacent normal tissues observed in scatterplots in section 5). A simple linear classifier (Matlab function `classify`) was trained on 10% of pixels in the areas outlined in each of the parametric maps as a

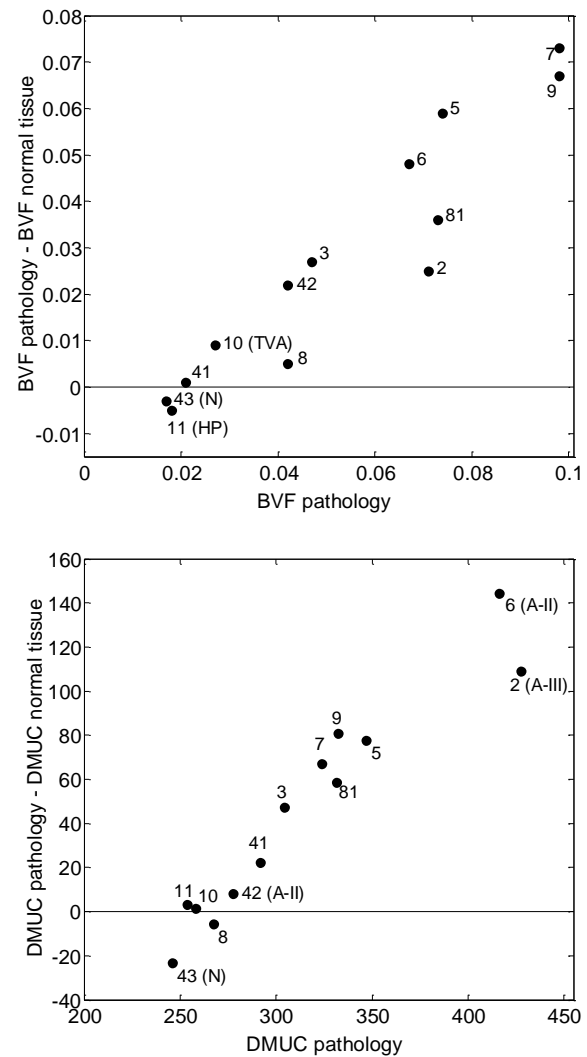


Fig. 11. Relationship between parameter values characterising a pathology against the difference between parameter values in pathological areas and the neighbouring normal tissue. Horizontal line depicts zero difference. Top plot: blood volume fraction; Bottom plot: thickness of mucosa.

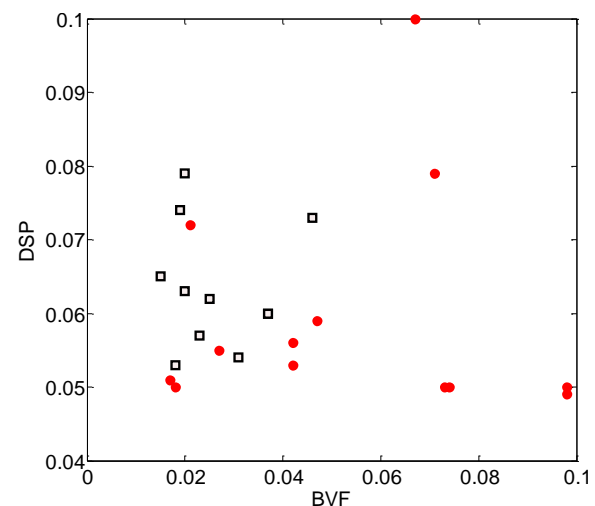


Fig. 12. Plot of BVF against DSP for the lesions (red dots) and for the neighbouring regions (black squares).

pathology and as a normal area (see B). The classifier was then applied to the parametric map data and its sensitivity (TPR), specificity (SPC) and positive predictive value (PPV) computed. Leave-one-out classification using jointly the training data derived from all the datasets resulted in the mean rates of TPR=0.40, SPC=0.28 and PPV=0.09. Classification using the training data derived from a given set gave TPR=0.85, SPC=0.78 and PPV=0.34. The results when using the training data jointly have confirmed that “normal tissue” cannot be treated as a homogenous entity across all the colon samples; none of the TPR, SPC or PPV indicates good selectivity. When using the training data specific to a given sample specificity is markedly improved, however the positive predictive value remains low. The main source of false positives are the valleys of the folds, many of which are likely to contain residual blood. Since the increase in the blood volume fraction is a main feature of malignant lesions these regions are classified as abnormalities. This is unlikely to be the case in *in vivo* images.

This classification experiment used unsophisticated methods, lacked separation between the training and testing data and was carried out on a small and diverse dataset. For these reasons its results are only indicative of the capabilities of the parametric maps to highlight the abnormal features. However, they provide tentative evidence suggesting that any future schemes should always consider abnormalities in the context of an individual patient and a segment of a gastrointestinal tract.

## VI. DISCUSSION

This paper has described a method for obtaining quantitative estimates of histological parameters from multispectral images of the colon and examined their potential for discriminating between normal and pathological tissues.

The method is based on model inversion. A forward model uses Monte Carlo simulation to compute reflectance spectra of colon tissue instances corresponding to varying levels of three mucosal parameters: blood volume fraction, density of scattering particles and thickness. Given an image spectrum the corresponding parameters are derived based on the closest match in the model. However, the resulting parametric maps cannot be guaranteed to be quantitatively correct because the analysis showed that the model is not strictly invertible, meaning that two different parameter sets could generate two almost identical spectra (see III.B). This is most likely the property of tissue reflectance under diffuse illumination rather than the result of using a particular modelling scheme or parameterisation. A pragmatic solution adopted in this work was to follow the model inversion by optimisation that in the ambiguous cases chose a parameter set that increased spatial smoothness of all three parametric maps whilst maintaining good spectral match. Other post-inversion methods that were examined but produced inferior results included a radial basis network, a back-propagating network, a K-nearest neighbour method and partial-least-squares regression. Whilst the

uncertainty in parametric maps remains, statistically the maps can be considered to be fairly representative of tissue histology (sections III.E and III.B). This was further confirmed by the observations and quantitative analysis of the real cases (sections V.A and V.B).

The issue of foremost importance in this work is the diagnostic potential of the parametric maps. Two possible applications with slightly different requirements are abnormality detection and differential diagnosis. In abnormality detection a tissue is scanned to identify any suspicious areas. It is essential that all, sensitivity, specificity and positive predictive value, are high so that no abnormality is missed and any false alarms are minimised. The preliminary classification experiment (V.B.6) as well as visual inspection of the parametric maps show clearly that at present the maps are not discriminative enough. However, high spatial sensitivity scores of (mean 0.88, range 0.75 - 1.00) indicate the potential of the maps in the inspection and staging of pathologies once found. For instance a small adenomatous polyp (~3mm) in Fig. 10B shows elevated levels of BVF and DSP, characteristic of an evolving tumour, whereas a hyperplastic polyp (which carry no risk of developing into the cancer) of a similar size in Fig. 10D has BVF and DSP levels in line with the surrounding tissue. Differentiation between hyperplastic and adenomatous polyps of small sizes is generally considered quite challenging [9]. As another example, all adenocarcinomas of grade II and above show elevated levels of mucosal thickness whereas those of grade I do not. Due to the very small number of samples used in this study the above examples do not constitute evidence that parametric maps can assist in differential diagnosis. However, they indicate that further study is justified.

There are several possible reasons for poor predictive value in an attempted classification. In the construction of a training sample the “surrounding tissue” class was assumed to be fairly uniform. This is clearly not the case. The baseline characteristics of the colon structure do vary from patient to patient, and from one part of the colon to the other. Colon samples used in this study originate from several different parts of the gastrointestinal track (Table 6). A larger study could determine whether the site-specific characterisation is possible. Individual differences due to age, gender and other factors are likely to be substantial. For this reason the absolute values of parameters are thought to be of less importance than their relative differences, especially when consistent with the known histological changes due to a pathology. Spatial distribution and pattern uniformity might also provide diagnostic clues. It is known that microvessels, collagen fibres and cell sizes tend to show more haphazard structure and less uniform sizes. Such micro-disorganisation may result in less uniform distribution of features in the parametric maps.

This study was carried out on excised tissue samples and different results, possibly more consistent across the subjects, should be expected from *in vivo* studies for the following reasons. During surgery and sample preparation the tissue

might have been traumatised by bruising or stretching with the resulting changes to its structure. Some of the changes were certainly due to tissue dehydration, i.e. loss of blood and water content, and the resulting shrinkage of the tissue. It was also observed that some free blood accumulated in pockets of colonic folds. Although formalin did not affect tissue imaging it might have changed tissue itself. The computation of parametric maps derived from *in vivo* data would eliminate these confounding factors. However, given that the optical properties of the model currently specified as constants are correct (Table 1) the differences between the *in vivo* and *ex vivo* model should be confined only to the ranges of variable parameters.

As noted in section V.B the normal colon tissue can show significant variations between individuals and between different colon segments. The parameter *differences* between the pathological regions and their surroundings are therefore likely to be of more importance than the absolute values. This suggests that multispectral imaging should be more appropriate than point spectroscopy in pathology identification.

It is important to stress that the interpretation of the spectra based on the physics of light interaction with tissue differs significantly from direct approaches to analysis in which statistical or pattern analysis techniques are applied to the spectra, without considering the process of their formation (e.g. [8] [9] [10]). Physics-based approaches, such as described in this paper or developed by Zonios *et al.* [11], can provide a histological interpretation of spectral features which makes them clinically more informative than statistical analysis of spectra.

## VII. CONCLUSIONS

The work described in this paper demonstrated that histological parametric maps derived from multispectral images show gross correspondence with histological features of mucosa characteristic of cancerous, pre-cancerous and non-cancerous colon lesions. The key signs of abnormality are the increase in the blood volume fraction and decrease in the density of scattering particles. Appropriately, these features could be observed even in small (several millimeters) neoplastic polyps but not in hyperplastic polyps. Higher grade tumours showed the increased thickness of the mucosa. Simple classification demonstrated that the above signs are highly sensitive to the presence of pathologies but their specificity and positive predictive value is low. The latter was attributed to the high variability of the normal colon tissues and to the use of excised samples rather than a living colon. However, in the case-by-case analysis differences in the values of the parameters characterising normal and histologically proven cancerous tissue were shown to be statistically significant suggesting that the method is capable of differentiating between the two tissue types.

The use of model inversion to compute parametric maps was shown to be ill-posed; approximately 10% of the

(discretised) model parameter vectors were found to have spectra differing by less than an estimated noise level. The subsequent use of optimisation with spatial smoothness constraint decreased the uncertainty of parameter recovery so that on the simulated data the Spearman's rank correlation coefficient  $\rho$  for the input and the recovered maps was 0.653 on average. With more data samples the use of Bayesian methods such as maximum a posteriori estimation may improve the accuracy of the parametric maps.

This preliminary study, on the use of a physics-based model of image formation to derive histologically meaningful information from multispectral images of the colon, has demonstrated the feasibility of the approach. The next step will be to validate the method on colon images collected *in vivo* from a variety of colon sections and pathologies. Fast hyperspectral imaging endoscopes that are being currently developed in a number of research laboratories are capable of providing the required input data [36] [37, 38]. Ultimately, "Optical techniques may permit immediate clinical diagnosis, removing the need for histological analysis. They may also improve the diagnosis of early colonic neoplasia." [1].

## ACKNOWLEDGMENT

The authors would like to thank Mr Tariq Ismail and Dr Nigel Suggett (Queen Elizabeth Hospital, Birmingham) for their help with the acquisition of endoscopic images.

## REFERENCES

- [1] J. Taylor, C. Kendall, N. Stone, and T. Cook, "Optical adjuncts for enhanced colonoscopic diagnosis," *British Journal of Surgery*, vol. 94, pp. 6-16, 2007.
- [2] F. Van Den Broek, P. Fockens, and E. Dekker, "Review article: new developments in colonic imaging," *Alimentary Pharmacology & Therapeutics*, vol. 26, pp. 91-99, 2007.
- [3] S. J. Preece and E. Claridge, "Spectral filter optimisation for the recovery of parameters which describe human skin," *IEEE Trans. Pattern Analysis and Machine Intelligence*, vol. 26, pp. 913-922, 2004.
- [4] I. B. Styles, A. Calcagni, E. Claridge, F. Orihuela-Espina, and J. M. Gibson, "Quantitative analysis of multi-spectral fundus images," *Medical Image Analysis*, vol. 10, pp. 578-597, Aug 2006.
- [5] A. Calcagni, J. M. Gibson, I. Styles, E. Claridge, and F. Orihuela-Espina, "Multispectral retinal image analysis: a novel non-invasive tool for retinal imaging," *Eye*, vol. 25, pp. 1562-1569, 2011.
- [6] D. Hidović-Rowe and E. Claridge, "Modelling and validation of spectral reflectance for the colon," *Physics in medicine and biology*, vol. 50, p. 1071, 2005.
- [7] E. Claridge, D. Hidović-Rowe, P. Taniere, and T. Ismail, "Quantifying mucosal blood volume fraction from multispectral images of the colon," in *Medical Imaging 2007: Physiology, Function, and Structure from Medical Images*, 2007, pp. 65110C1 - 65110C8.
- [8] J. R. Mourant, I. J. Bigio, J. D. Boyer, T. M. Johnson, J. Lacey, A. G. Bohorofoush III, and M. H. Mellow, "Elastic scattering spectroscopy as a diagnostic tool for differentiating pathologies in the gastrointestinal tract: preliminary testing," *Journal of Biomedical Optics*, vol. 1, pp. 192-199, 1996.
- [9] Z. Ge, K. T. Schomacker, and N. S. Nishioka, "Identification of colonic dysplasia and neoplasia by diffuse reflectance spectroscopy and pattern recognition techniques," *Applied Spectroscopy*, vol. 52, pp. 833-839, 1998.
- [10] M. Sambongi, M. Igarashi, T. Obi, M. Yamaguchi, N. Ohyama, M. Kobayashi, Y. Sano, S. Yoshida, and K. Gono, "Analysis of spectral reflectance using normalization method from endoscopic spectroscopy system," *Optical Review*, vol. 9, pp. 238-243, 2002.



- [11] G. Zonios, L. T. Perelman, V. Backman, R. Manoharan, M. Fitzmaurice, J. Van Dam, and M. S. Feld, "Diffuse Reflectance Spectroscopy of Human Adenomatous Colon Polyps *in Vivo*," *Applied Optics*, vol. 38, pp. 6628-6637, 1999.
- [12] J. Galeano, R. Jolivot, Y. Benezeth, F. Marzani, J.-F. Emile, and D. Lamarque, "Analysis of Multispectral Images of Excised Colon Tissue Samples Based on Genetic Algorithms," in *Signal Image Technology and Internet Based Systems (SITIS), 2012 Eighth International Conference on*, 2012, pp. 833-838.
- [13] A. Pierangelo, A. Benali, M.-R. Antonelli, T. Novikova, P. Validire, B. Gayet, and A. De Martino, "Ex-vivo characterization of human colon cancer by Mueller polarimetric imaging," *Optics Express*, vol. 19, pp. 1582-1593, 2011.
- [14] T. Yoshida, H. Inoue, S. Usui, H. Satodate, N. Fukami, and S.-e. Kudo, "Narrow-band imaging system with magnifying endoscopy for superficial esophageal lesions," *Gastrointestinal Endoscopy*, vol. 59, pp. 288-295, 2004.
- [15] R. Kiesslich, M. Goetz, M. Vieth, P. R. Galle, and M. F. Neurath, "Technology insight: confocal laser endoscopy for in vivo diagnosis of colorectal cancer," *Nature Clinical Practice Oncology*, vol. 4, pp. 480-490, 2007.
- [16] <http://www.maunakeatech.com/>.
- [17] G. R. Lloyd, C. Kendall, T. Cook, N. Shepherd, and N. Stone, "Histological imaging of a human colon polyp sample using Raman spectroscopy and self organising maps," *Vibrational Spectroscopy*, 2012.
- [18] B. Banerjee, T. Renkoski, L. R. Graves, N. S. Rial, V. L. Tsikitis, V. Nfonso, J. Pugh, P. Tiwari, H. Gavini, and U. Utzinger, "Tryptophan autofluorescence imaging of neoplasms of the human colon," *Journal of Biomedical Optics*, vol. 17, pp. 016003-1-016003-7, 2012.
- [19] B. J. Vakoc, D. Fukumura, R. K. Jain, and B. E. Bouma, "Cancer imaging by optical coherence tomography: preclinical progress and clinical potential," *Nature Reviews Cancer*, vol. 12, pp. 363-368, 2012.
- [20] N. A. Shepherd, B. F. Warren, G. T. Williams, J. K. Greenston, G. Y. Lauwers, and M. R. Novelli, *Morson and Dawson's Gastrointestinal Pathology*: Wiley-Blackwell, 2012.
- [21] S. L. Robbins, V. Kumar, A. K. Abbas, R. S. Cotran, and N. Fausto, *Robbins and Cotran pathologic basis of disease*: WB Saunders Company, 2010.
- [22] L. Wang, S. L. Jacques, and L. Zheng, "MCML—Monte Carlo modeling of light transport in multi-layered tissues," *Computer Methods and Programs in Biomedicine*, vol. 47, pp. 131-146, 1995.
- [23] L. Wang and S. L. Jacques, "Monte Carlo modeling of light transport in multi-layered tissues in standard C," *The University of Texas, MD Anderson Cancer Center, Houston*, 1992.
- [24] E. Claridge and S. J. Preece, "An inverse method for the recovery of tissue parameters from colour images," in *Information Processing in Medical Imaging (IPMI)*, 2003, pp. 306-317.
- [25] J. Besag, "On the statistical analysis of dirty pictures," *Journal of the Royal Statistical Society. Series B (Methodological)*, pp. 259-302, 1986.
- [26] S. Z. Li, *Markov random field modeling in image analysis*: Springer, 2009.
- [27] A. Blake, P. Kohli, and C. Rother, *Markov random fields for vision and image processing*: The MIT Press, 2011.
- [28] N. Komodakis, N. Paragios, and G. Tziritas, "MRF optimization via dual decomposition: Message-passing revisited," in *Computer Vision, 2007. ICCV 2007. IEEE 11th International Conference on*, 2007, pp. 1-8.
- [29] P. Kohli and P. H. Torr, "Robust higher order potentials for enforcing label consistency," *International Journal of Computer Vision*, vol. 82, pp. 302-324, 2009.
- [30] C. Wang, N. Komodakis, and N. Paragios, "Markov Random Field modeling, inference & learning in computer vision & image understanding: A survey," *Computer Vision and Image Understanding*, 2013.
- [31] J. H. Kappes, B. Andres, F. A. Hamprecht, C. Schnörr, S. Nowozin, D. Batra, S. Kim, B. X. Kausler, J. Lellmann, and N. Komodakis, "A comparative study of modern inference techniques for discrete energy minimization problems," in *Proceedings of the IEEE Conference on Computer Vision and Pattern Recognition (CVPR)*, 2013.
- [32] D. Hidović-Rowe, J. E. Rowe, and M. Lualdi, "Markov models of integrating spheres for hyperspectral imaging," *Applied Optics*, vol. 45, pp. 5248-5257, 2006.
- [33] P. Maxim, J. Carson, D. Benaron, B. Loo Jr, L. Xing, A. Boyer, and S. Friedland, "Optical detection of tumors in vivo by visible light tissue oximetry," *Technology in Cancer Research & Treatment*, vol. 4, p. 227, 2005.
- [34] J. Turnay, N. Olmo, J. G. Gavilanes, and M. A. Lizarbe, "Collagen metabolism in human colon adenocarcinoma," *Connective Tissue Research*, vol. 23, pp. 251-260, 1989.
- [35] Y. Furuya and T. Ogata, "Scanning electron microscopic study of the collagen networks of the normal mucosa, hyperplastic polyps, tubular adenoma, and adenocarcinoma of the human large intestine," *The Tohoku Journal of Experimental Medicine*, vol. 169, p. 1, 1993.
- [36] R. T. Kester, N. Bedard, L. Gao, and T. S. Tkaczyk, "Real-time snapshot hyperspectral imaging endoscope," *Journal of Biomedical Optics*, vol. 16, pp. 056005-056005-12, 2011.
- [37] T. Arnold, M. De Biasio, and R. Leitner, "High-sensitivity hyperspectral video endoscopy system for intra-surgical tissue classification," in *Sensors, 2010 IEEE*, 2010, pp. 2612-2615.
- [38] D. Yi and L. Kong, "Novel instrumentation of multispectral imaging technology for detecting tissue abnormality," in *SPIE Optical Engineering+ Applications*, 2012, pp. 84980J-84980J-6.